PHYSICAL REVIEW MATERIALS **5**, 015001 (2021)

High-pressure synthesis of Ba_2RhO_4, a rhodate analog of the layered perovskite Sr-ruthenate

I. Kurata,[1,2] José A. Flores-Livas,[3,4] H. Sugimoto,[2] H. Takahashi,[1,5] H. Sagayama,[6] Y. Yamasaki,[7] T. Nomoto,[2] R. Arita,[2] and S. Ishiwata[1,2,5,*]

[1]*Division of Materials Physics, Graduate School of Engineering Science, Osaka University, Osaka 560-8531, Japan*
[2]*Department of Applied Physics, University of Tokyo, Tokyo 113-8656, Japan*
[3]*Dipartimento di Fisica, Università di Roma La Sapienza, Piazzale Aldo Moro 5, I-00185 Roma, Italy*
[4]*RIKEN Center for Emergent Matter Science, 2-1 Hirosawa, Wako 351-0198, Japan*
[5]*Center for Spintronics Research Network (CSRN), Graduate School of Engineering Science, Osaka University, Osaka 560-8531, Japan*
[6]*Institute of Materials Structure Science, High Energy Accelerator Research Organization, Tsukuba, Ibaraki 305-0801, Japan*
[7]*Research and Services Division of Materials Data and Integrated System (MaDIS), National Institute for Materials Science (NIMS), Ibaraki, Tsukuba 305-0047, Japan*

(Received 13 October 2020; accepted 23 December 2020; published 26 January 2021)

A layered perovskite-type oxide Ba_2RhO_4 was synthesized by a high-pressure technique with the support of convex-hull calculations. The crystal and electronic structure were studied by both experimental and computational tools. Structural refinements for powder x-ray diffraction data showed that Ba_2RhO_4 crystallizes in a K_2NiF_4-type structure, isostructural to Sr_2RuO_4 and Ba_2IrO_4. Magnetic, resistivity, and specific-heat measurements for polycrystalline samples of Ba_2RhO_4 indicate that the system can be characterized as a correlated metal. Despite the close similarity to its Sr_2RuO_4 counterpart in the electronic specific-heat coefficient and the Wilson ratio, Ba_2RhO_4 shows no signature of superconductivity down to 0.16 K. Whereas the Fermi surface topology has reminiscent pieces of Sr_2RuO_4, an electronlike e_g-($d_{x^2-y^2}$) band descends below the Fermi level, making this compound unique also as a metallic counterpart of the spin-orbit coupled Mott insulator Ba_2IrO_4.

DOI: 10.1103/PhysRevMaterials.5.015001

I. INTRODUCTION

Layered perovskite-type oxides A_2MO_4 (where A denotes a rare-earth metal or alkaline earth metal, and M is a transition metal) have been extensively studied as two-dimensional correlated electron systems showing exotic electronic properties. This is typified by $La_{2-x}Sr_xCuO_4$ and Sr_2RuO_4 showing unconventional superconductivity [1–5], and Sr_2CoO_4 showing ferromagnetic and metallic behavior [6]. Because of the close analogy to La_2CuO_4, Sr_2IrO_4 has recently attracted a great deal of attention [7–9]. The ground state of Sr_2IrO_4 has been described as a spin-orbit coupled Mott insulating state with antiferromagnetic ordering [10]. In A_2MO_4, the symmetry and local distortion of the M-O square lattice, which depend on the size of the A-site ion, seem to play an important role for their electronic ground states. For instance, Sr_2RuO_4 has tetragonal symmetry with straight Ru-O-Ru bonds, whereas Ca_2RuO_4, which is known as an antiferromagnetic Mott insulator, has large distortion of the Ru-O-Ru bonds [11]. Recently, Ba_2IrO_4 has been synthesized by a high-pressure technique and found to be tetragonal with straight Ir-O-Ir bonds, which are in contrast to those of Sr_2IrO_4 with orthorhombic distortion [12]. Reflecting the absence of lattice distortion, the magnetic ground state of Ba_2IrO_4 is free from the spontaneous magnetic moment caused by the Dzyaloshinskii-Moriya interaction, unlike the case of Sr_2IrO_4.

As mentioned above, Sr_2RuO_4, which has a $4d^4$ electronic configuration of Ru^{4+} with moderate electron correlation, and Ba_2IrO_4, which has a $5d^5$ electronic configuration of Ir^{4+} with strong spin-orbit coupling (SOC), share the same tetragonal layered perovskite-type structure but show contrasting ground states. Therefore, it is tempting to explore novel electronic states in similar compounds. Following this viewpoint, we focus on the rhodium analog with a $4d^5$ electronic configuration of Rh^{4+} with moderate electron correlation and SOC [13–16]. So far, solid solutions between Sr_2RhO_4 and the known compounds such as $Sr_2Rh_{1-x}Ir_xO_4$ [17] and $Sr_{2-x}La_xRhO_4$ [18] have been studied. However, these oxides have a lattice distortion unlike Sr_2RuO_4 and Ba_2IrO_4 with straight M-O-M bonds, which can be critical for the emergence of novel electronic states.

In this work, we achieved the high-pressure synthesis of a layered perovskite rhodate Ba_2RhO_4, and we characterized its structural, magnetic, and electronic properties. From Rietveld refinements of the synchrotron x-ray diffraction data, Ba_2RhO_4 was found to crystallize in the tetragonal space group ($I4/mmm$), being isostructural with Sr_2RuO_4. In addition to this first member of Ruddlesden-Popper phases $Ba_{n+1}Rh_nO_{3n+1}$ with $n = 1$, other possible formations of the other phases with $n = 2$, 3, and ∞ (perovskite phase) under high pressures are also predicted in terms of their formation enthalpy. Although the signature of superconductivity has not been found at low temperatures down to 0.16 K, the close similarity to the Sr_2RuO_4 counterpart will be discussed.

---

[*] Corresponding author: ishiwata@mp.es.osaka-u.ac.jp

II. METHOD

A. Experimental details

Polycrystalline samples of Ba_2RhO_4 were prepared by the solid-state reaction with a high-pressure technique using a cubic-anvil-type high-pressure apparatus (METEORITE). The stoichiometric mixture of BaO_2 (99.9%, Furuuchi Chemical Co., Ltd.) and Rh metal powder (99.96%, Furuya Metal Co., Ltd.) was encapsulated in a platinum capsule with a diameter of 4 mm in a glove box with a high-purity argon atmosphere. After taking the sample in a platinum capsule out of the glove box, it was quickly mounted in a pyrophyllite cell with a BN sleeve and a carbon heater. Then, the sample was heated up to 1350–1400 °C within 5 min and kept for 30 min at 8 GPa, followed by quenching to room temperature before the pressure was released. The polycrystalline sample of Ba_2RhO_4 was obtained as a dense and black pellet. As the sample is sensitive to air and moisture, it was kept in a glove box. The purity of the sample was checked by powder x-ray diffraction with Cu $K\alpha$ radiation (BRUKER new D8). The data for structure refinements were collected as well, by synchrotron powder x-ray diffraction with a wavelength of 0.689 75 Å at BL-8B, Photon Factory, KEK, Japan. The diffraction data were analyzed using the Rietveld refinement using RIETAN-FP [19]. The resistivity and specific heat were measured by a Physical Property Measurement System (PPMS). The resistivity measurement below 2 K was performed by the Adiabatic Demagnetization Refrigerator (ADR) option for PPMS. Magnetic susceptibility data were collected by a superconducting quantum interference device magnetometer.

B. Computational details

The scan of enthalpically low configurations from constructed model crystals was performed using structure exploration tools as in Ref. [20]. For the convex hull, all structural relaxations at different pressures were evaluated within DFT at the level of the Perdew-Burke-Ernzerhof (PBE) [21] approximation to the exchange-correlation functional. A plane-wave basis set with a cutoff energy of 900 eV was used to expand the wave functions together with the projector augmented wave (PAW) method as implemented in the Vienna ab initio Simulation Package (VASP) [22]. Structures in the convex hull construction were converged to less that 2 meV $Å^{-1}$. All electronic band structures and magnetic properties were calculated using the full-potential linearized augmented plane-wave (FP-LAPW) method as implemented within the ELK code [23,24]. We took into account spin-orbit coupling (SOC) and performed a fully noncollinear LSDA magnetic calculation (we searched for possible stable magnetic configurations in case the system was magnetic). For coherence, in the last step, all volumes were optimized using the LDA functional. Finally, the potential and density were expanded in plane waves with a cutoff of $|\mathbf{G}| = 24/a_0$, and we set $R_{\min} \times |\mathbf{G}+\mathbf{k}|$ to 9, where $R_{\min}$ is the smallest muffin-tin radius. The maximum angular momentum l for the expansion of the wave function inside the muffin tins was set to 12. k-point grids were chosen with a minimum allowed spacing between k points of 0.15 in units of $Å^{-1}$, equivalent to $14 \times 14 \times 8$ or more.

TABLE I. Structural parameters for Ba_2RhO_4. Space group $I4/mmm$ (No. 139). $a = b = 4.0063(2)$ Å, $c = 13.2966(8)$ Å, $V = 213.42(2)$ $Å^3$. Reliability factors: $R_{wp} = 2.486$, $S = 1.95$.

Atoms	Site	x	y	z	B (Å2)
Ba	4*e*	0	0	0.3556(1)	0.60(2)
Rh	2*a*	0	0	0	0.24(3)
O1	4*c*	0	0.5	0	1.0(1)
O2	4*e*	0	0	0.1522(7)	1.0(1)

III. RESULTS

A. Formation enthalpy of the 2-1-4 phase of Ba-Rh-O

Figure 1 shows the convex hull of enthalpy formation calculated for stoichiometries between BaO and RhO_2, which can be found in the ternary phase diagram of Ba-Rh-O (see Fig. S1 [25]). At ambient pressure, the formation energy suggests that compositions such as Ba_2RhO_4 (2-1-4) and $BaRhO_3$ (1-1-3) are likely to be accessible to synthesis. Under pressures above 5 GPa, the 2-1-4 phase lowers its enthalpy, and it is favorable with respect to the 1-1-3 phase ($BaRhO_3$), suggesting that it could be stabilized upon the application of pressure. Our calculations also show that the Ruddlesden-Popper phases ($Ba_{n+1}Rh_nO_{3n+1}$) with bilayer ($n = 2$) and trilayer ($n = 3$) structures are not stable even at high pressures up to 20 GPa. Completing the Ruddlesden-Popper phase with $n = \infty$, the enthalpy reaches the highest value and matches the 1-1-3 in its cubic-perovskite phase. It is worth mentioning that in our results, the lowest enthalpy structure for the 1-1-3 phase is disputed between the hexagonal 6H and 4H structure motif below 20 GPa, and that only at very high pressures does the cubic perovskite phase dominate. Motivated by these findings, a high-pressure synthesis was carried out to find the stable 2-1-4 stoichiometry of the Ba-rhodate family (Sec. II A). We only attempted the synthesis of the 2-1-4 compositions, and after optimizing the synthesis conditions, structural and electrical measurements were carried out.

B. Structural properties

Figure 2(c) shows the powder x-ray diffraction pattern of Ba_2RhO_4, which was indexed on the basis of the tetragonal K_2NiF_4-type structure with space group $I4/mmm$[$a = 4.0063(2)$, $c = 13.2966(8)$ Å]. The model of the Rietveld analysis is summarized in Table I, and the crystal structure is shown in Fig. 2(a). Another possible structural model with space group $I4_1/acd$, which allows rotation of the RhO_6 octahedra as in the case of Sr_2RhO_4, can be ruled out by the absence of the visible reflections, which are allowed and forbidden for the models with $I4/mmm$ and $I4_1/acd$, respectively (see Fig. S2 [25]). Indeed, we confirmed that the reliability factors for $I4_1/acd$ are larger than for $I4/mmm$ (see Table SI [25]). The Rh-O bond lengths 2.00–2.02 Å refined for $I4/mmm$ are fairly comparable to the value expected for that of Rh^{4+}-O^{2-}. On the other hand, as shown in Fig. 2(b), the

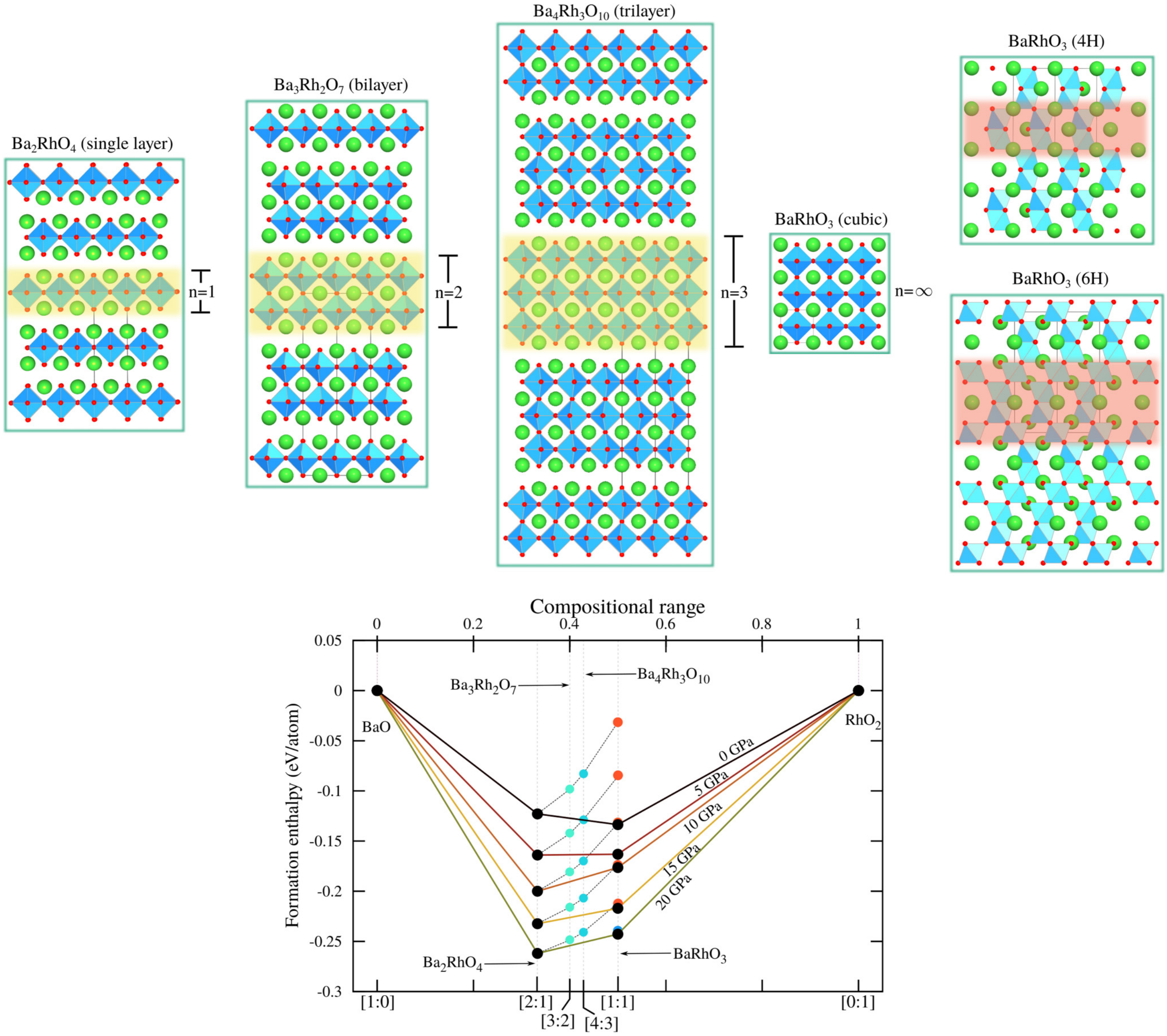

FIG. 1. Bottom panel: convex hull of enthalpy formation calculated for stoichiometries between BaO and RhO_2 at selected pressures up to 20 GPa. For readability, the abscissa in the top shows composition range and in the bottom it shows composition ratio. Solid-black points represent stable compositions, and empty colored circles represent unstable ones. The crystal structure of stable and unstable phases is shown in the top and presented as the Ruddlesden-Popper sequence ($Ba_{n+1}Rh_nO_{3n+1}$). Lower formation enthalpy means the structure and composition are thermodynamically accessible to synthesis. For each pressure, the line of stability is indicated. We can rule out the synthesis of $n = 1$ and 2 at the studied pressures. The prediction that the 2-1-4 phase is stabilized upon pressure is confirmed in our experiments.

refined Ba-O lengths are significantly shorter than the value 2.87 Å expected for the bond length between Ba^{2+} (1.47 Å for the ninefold coordination) and O^{2-} ions (1.40 Å for the sixfold coordination) [26], indicating the compressed (over bonding) nature of the Ba-O bond. This feature points toward the metastable nature of the crystalline phase of Ba_2RhO_4 at ambient pressure.

C. Electrical resistivity, magnetic susceptibility, and specific-heat capacity

The electrical resistivity and magnetic susceptibility as a function of temperature for Ba_2RhO_4 are shown in Fig. 3. Below 50 K, the electrical resistivity deviates from the T^2 dependence, expected for a Fermi liquid, and resistivity evolves as $\rho = \rho_0 + AT^\alpha$ with $\rho_0 = 4.25$ mΩ cm, $A = 9.24$ $\mu\Omega\,\text{cm/K}^2$, and $\alpha = 1.52$, which is in contrast to Sr_2RhO_4 with α comparable to or even larger than 2. Despite the apparent anomaly in α implying a non-Fermi-liquid state, we cannot put into evidence its origin due to the polycrystalline nature of the material. It is also evident that we cannot conduct studies to rule out the possibility of anisotropy in the electrical resistivity inherent to the layered structure. In fact, the residual resistivity ρ_0 is relatively large as reported for the polycrystalline sample of Sr_2RhO_4 [27], presumably reflecting the grain boundary scattering and the layered structure. Interestingly, even decreasing the temperature down to 160 mK, no superconducting transition was observed [see the

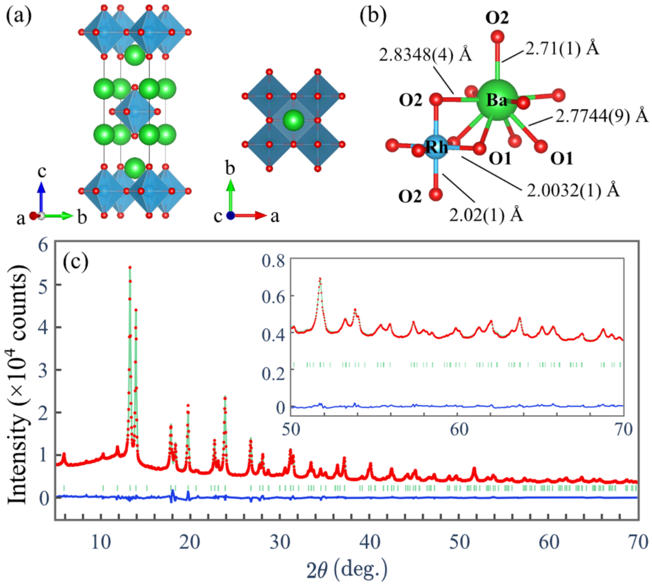

FIG. 2. (a) Crystal structure of Ba_2RhO_4 and (b) a schematic representation of the local structure with bond lengths around the Rh and Ba atoms. (c) Observed (red crosses), calculated (green line), and differential (blue line) synchrotron x-ray diffraction patterns. The green tick marks indicate the calculated peak positions.

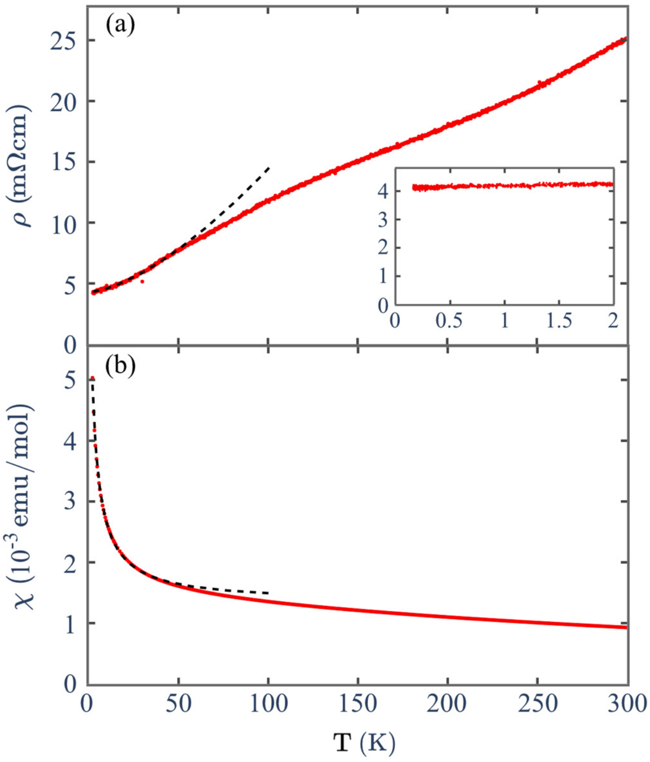

FIG. 3. The temperature dependence of (a) electrical resistivity and (b) magnetic susceptibility for Ba_2RhO_4. The green dashed line shows the fitting of the experimental data with $\rho = \rho_0 + AT^\alpha$ and $\chi = \chi_0 + C/(T+\theta)$ below 50 K. The inset of (a) shows no superconducting signals down to 0.16 K.

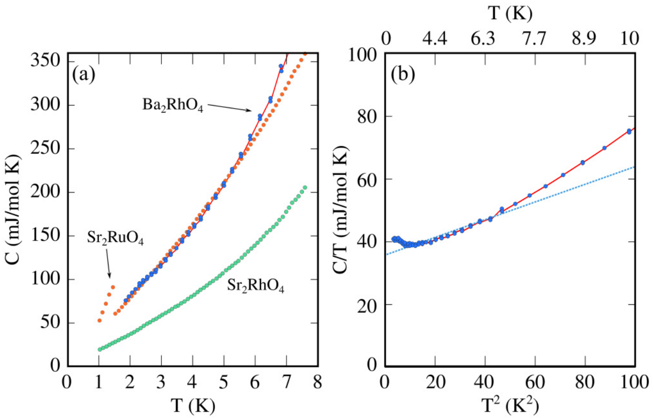

FIG. 4. (a) Temperature dependence of the specific heat for Ba_2RhO_4 (blue dots), and the reported specific heat of Sr_2RuO_4 (red dots) and Sr_2RhO_4 (green dots). (b) T^2 dependence of specific heat divided by temperature for Ba_2RhO_4 (blue dots). The blue dashed line shows the fitting of the experimental data with $T/C = \gamma + \beta T^2$ between 2.0 and 7.5 K.

inset of Fig. 3(a)]. As shown in Fig. 3(b), a Curie-like tail is distinguishable below 50 K, and fitting the magnetic susceptibility with the expression $\chi = \chi_0 + C/(T+\theta)$ gives $\chi_0 = 1.33 \times 10^{-3}$ emu/mol, $C = 1.63 \times 10^{-2}$ emu/mol K, and $\theta = -2.55$ K. The C value is close to zero, and no signal of magnetic transition is visible, indicating that a localized magnetic moment is absent in Ba_2RhO_4.

The specific-heat capacity of our Ba_2RhO_4 samples is shown in Fig. 4 and is compared to the reported specific-heat capacities of Sr_2RuO_4 and Sr_2RhO_4 [14,27]. The expected dominance of the linear electronic term is seen for both Ba_2RhO_4 and Sr_2RuO_4 below approximately 7 K. Between 2.0 and 7.5 K, the specific heat follows the equation $C/T = \gamma + (12/5)\pi^4 N R \Theta_D^3 T^2 (R = 8.31\ \ \text{J/mol K}$ and $N = 1)$, where γ and Θ_D represent an electronic specific-heat coefficient and Debye temperature, respectively. Using this relation, we obtained the values of $\gamma = 36.56$ mJ/mol K^2 and $\Theta_D = 360$ K. The Debye temperature is comparable to that obtained by our first-principles calculations (~320 K) and that of Sr_2RuO_4 (~410 K) [28]. The electronic specific heat is as large as that of Sr_2RuO_4 (~39mJmol) [3], implying that the electron correlation enhances the effective mass of conduction electrons. Here, we estimated the Wilson ratio R_w using the following expression:

$$R_w = \frac{\pi^2 k_B^2}{3\mu_B^2}\frac{\chi_0}{\gamma}.$$

The estimated R_w (= 2.64) is comparable to or even larger than the reported ones for Sr_2RuO_4 (~1.9) and Sr_2RhO_4 (~2.3), which are regarded as clean correlated electron metals [14,29]. One should notice that the specific heat follows the above equation only in the narrow temperature range. Although the origin of the deviation at low temperature is elusive, the deviations below 4 and above 7 K may suggest an electronic instability that violates the current Debye model.

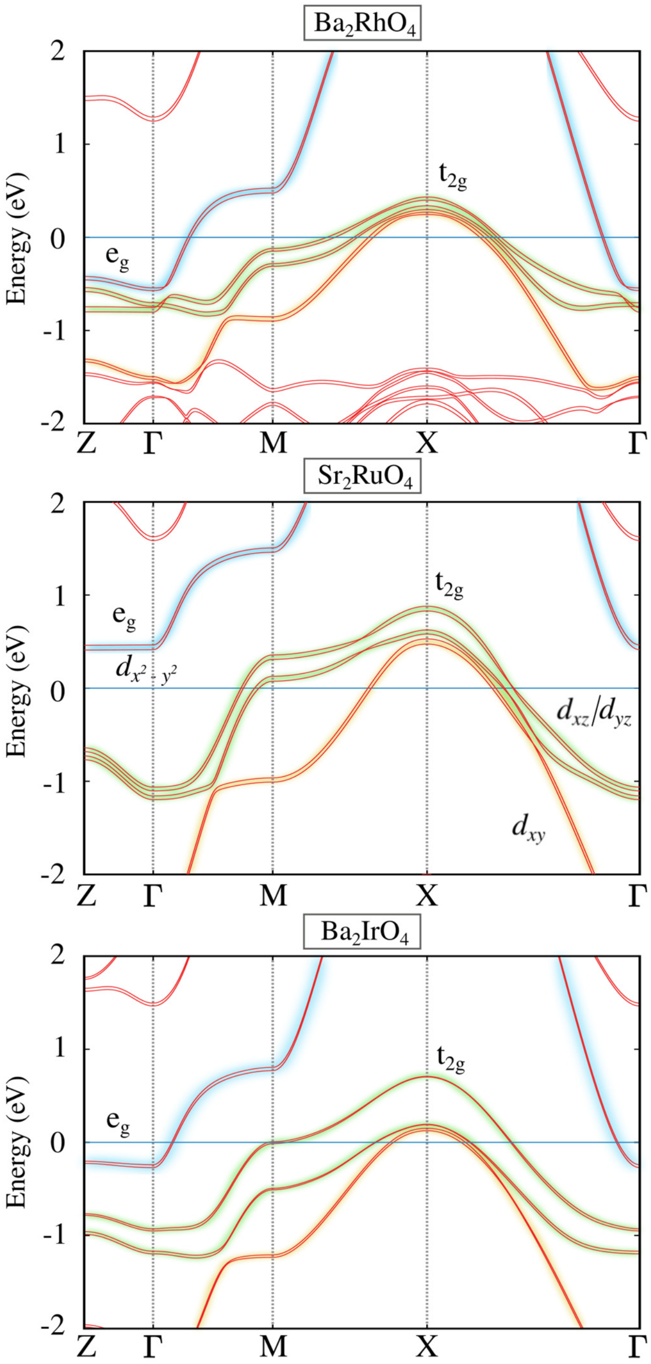

FIG. 5. Full-potential DFT-LSDA band structure including spin-orbit coupling along selected high-symmetry points at zero pressure. For comparison with the band structure of Sr_2RhO_4, see Fig. S6 [25].

D. Band structure and Fermi surface

Knowing that the 2-1-4 composition of Ba-Rh-O crystallizes in a layered-type structure similar to the 5d counterpart, Ba_2IrO_4, and the 4d counterpart, Sr_2RuO_4, it is interesting to compare the electronic band structure near the valence energy among these materials. The Kohn-Sham band structure of Ba_2RhO_4 calculated within the local spin density approximation (LSDA) and including SOC (LSDA + SO) is shown in Fig. 5. To have a meaningful comparison, we used their theoretical LDA-volume and assumed a K_2NiF_4-type structure for all cases. The band-structure calculation, at the level of theory employed here, evidences a metallic and nonmagnetic character for Ba_2RhO_4 (see Table SII [25]), which is in agreement with our resistivity and magnetic measurements (see the calculated density of states presented in Fig. S3 [25]). The case of Sr_2RuO_4, a prototypical system in manifolds, has been characterized in detail, and our calculations agree with the reported band structure for this system [30–33]. Ba_2IrO_4 is an interesting case in which basal-plane antiferromagnetism has been reported [12,34–37] at low temperatures, and a Mott insulator transition is driven by the SOC [38]. While the level of theory to treat this system is beyond the current theory employed in this work, in a simplified picture we wanted to compare with the energy bands on the 5d counterpart. The orbital character and the electronic symmetry of the bands are depicted as follows; the t_{2g}-dominated bands (d_{xy}, d_{xz}, and d_{yz}) are in yellow and green, and the e_g ($d_{x^2-y^2}$) bands are shown in blue.

As shown in Fig. 5, the electronic structure of Ba_2RhO_4 is closely related to that of Sr_2RuO_4, which has attracted a lot of attention for its possibility to emerge as a spin-triplet superconductor. However, the latest evidence suggests to disregard the chiral p-wave nature of the superconducting state of Sr_2RuO_4 [5,39–41]. On the other hand, our material, Ba_2RhO_4, has appealing differences evident around the Γ-point, where the e_g electron pocket descends the Fermi level, which is also found in Ba_2IrO_4 (using DFT-LSDA theory). A simple interpretation arises by looking at the position of the Fermi level in those systems, i.e., the electron counting of d bands in Ba_2RhO_4 is expected to be one more than that in Sr_2RuO_4. Looking at the t_{2g}-dominated bands among the three compounds, and comparing to the NO-SOC bands (not shown), we can conclude that SOC plays an important role in describing the splitting of d_{xz}/d_{yz} bands for the three compounds, while more marked differences arise for Sr_2RuO_4 and Ba_2IrO_4. Another noticeable difference is on the splitting and the width of t_{2g}-dominated bands for Sr_2RuO_4, two times larger as compared to Ba_2RhO_4. In our DFT optimizations, we find both Sr and Ba in the 2-1-4 phase to have a similar c/a ratio. As shown in Fig. S5 [25], we confirm that the difference emerges from the volume (density) and not directly from the c/a ratio (for comparable pressures).

Furthermore, in Ba_2IrO_4, the Mott insulator transition is driven by strong SOC, an effect that raises the bands opening a small band gap through a moderate Coulomb interaction. Although Ba_2RhO_4 is isoelectronic and isostructural with Ba_2IrO_4, such a gap opening is hampered by the reduced SOC. Thus, $Ba_2Rh_{1-x}Ir_xO_4$ with the tetragonal structure can be an ideal system to investigate the SOC-induced metal-insulator transition. As mentioned above, Ba_2RhO_4 is of peculiar interest, as it not only possesses inherent bands from the Ru counterpart, but it also shares similar electron bands from the 5d Ir. These feature places Ba-rhodate as strategic material that links the physics of 5d-oxides with 4d with a metallic character [42].

Understanding the topology of the Fermi surface of Ba_2RhO_4 is important to unravel the nature of electrons in the normal phase and possibly to shed light on the superconducting mechanism. The top panels in Fig. 6 show a

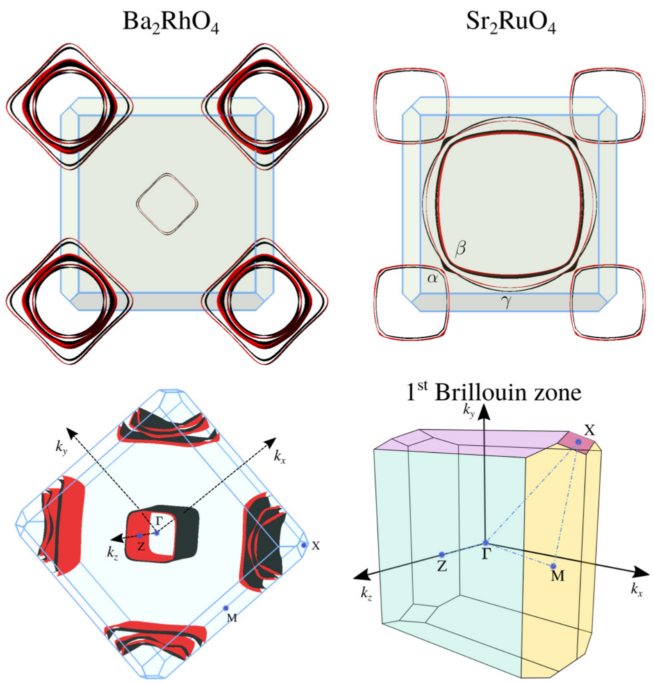

FIG. 6. DFT-LSDA Fermi surfaces including spin-orbit coupling for Ba_2RhO_4 and Sr_2RuO_4. Two-dimensional projections are along the k_z vector. The first Brillouin zone and selected high-symmetry points for the structure with $I4/mmm$ are shown.

two-dimensional Fermi surface of Ba_2RhO_4 and Sr_2RuO_4 [43,44]. The left bottom panel includes a three-dimensional cut, and on the right is shown the first Brillouin zone for the $I4/mmm$ crystal as a reference. The Fermi surface of Sr_2RuO_4 has been intensively investigated, both experimentally and theoretically [30–33]. *Ab initio* calculations based on the local-density approximation qualitatively reproduce the Fermi surface topology, provided that the SOC is taken into account. Our calculation reproduces the well-studied Fermi surface of Sr_2RuO_4, and it also confirms that striking differences in the Fermi surface of Ba_2RhO_4 emerged. These difference are ascribed to the d-electron counting, and the electron pocket with e_g symmetry that pins below the Fermi level (see Fig. 5). It should be noted that the squarelike tubular sheets along with X-Γ line can be regarded as a quasi-one-dimensional Fermi surface potentially yielding a nesting instability. More recently, LDA+DMFT (local-density approximation + dynamical mean-field theory) calculations have emphasized the interplay of Coulomb interaction and t_{2g} crystal field and the role of Hund's rule coupling [45–47]. In addition, laser-based angle-resolved photoemission spectroscopy revealed the importance of SOC in Sr_2RuO_4, and the self-energy estimations [48] for the β- and γ-sheets were found to display a significant angular dependence [32]. In this study, we did not perform calculations with higher theory beyond standard DFT, hence we cannot rule out that similar effects are present in Ba_2RhO_4.

Finally, we also performed electron-phonon calculations for Ba_2RhO_4 using perturbation theory. The calculated phonon dispersion is shown in Fig. S4 [25]. The normal-state Eliashberg spectral function was adopted to estimate λ (the dimensionless strength of the electron-phonon coupling) and the phonon average $\omega_{\log}$. These calculations reveal a weak BCS superconductor, and indeed our estimation of T_c is well below 0.1 K, in agreement with the absence of any hint of superconductivity down to 0.16 K in our experiments. To find the superconducting phase of Ba_2RhO_4, one might consider the possibility to further tune the electronic bands by applying pressure or by doing doping substitution, as recently reported for $Sr_{2-x}La_xRhO_4$ with a metal-insulator transition driven by a Lifshitz transition [18]. To gain insight into the pressure dependence of the bands, we also verified the dependence of the electronic structure under isotropic compression, from 1 to 20 GPa. Ba_2RhO_4 remains metallic well above 20 GPa, and the bands do not show any drastic change. The necessary pressure required to do a sizable change in the electronic structure is beyond 50 GPa. However, phase decomposition and other enthalpic phases might become more favorable. Another option is to tune the bands with anisotropic pressure, i.e., due to the dimensionality of the layered perovskite phase, strain engineering via the growth of thin films is very attractive to search for the superconducting phase, proving that a synthetic route other than the current high pressure exists.

IV. CONCLUSIONS

Using a high-pressure technique, a layered perovskite-type oxide Ba_2RhO_4 was synthesized and quenched to ambient conditions, which was supported by the convex hull calculations. The crystal and electronic structure were characterized by both experimental and theoretical works. Ba_2RhO_4 indeed shares many of the same interesting properties as Sr_2RuO_4, including the layered structure, specific heat, magnetic properties, and overall electronic features. The magnetic and resistivity measurements indicate that the system can be characterized as a correlated metal. Interestingly, the material does not show signs of superconductivity down to 0.16 K, which is supported by the theoretical estimation of the electron-phonon coupling. While the Fermi surface topology has pieces reminiscent of its Sr_2RuO_4 counterpart, one of the contrasting features in Ba_2RhO_4 is the presence of an electron e_g ($d_{x^2-y^2}$) band placed below the Fermi level, reflecting the increase in the d-electron counting. This feature provides a clue to discuss the role of electron correlation on the stabilization of a SOC-driven Mott insulating state in the isoelectronic and isostructural counterpart Ba_2IrO_4. The layered 2-1-4 perovskite phase [49] adds new possibilities to characterize 4d-electron physics, and bridges to the 5d-electron that is driven by SOC effects to Mott insulators [50]. The anomalous increase in the specific heat capacity below 4 K and the absence of superconductivity will be the subject of future work, conceding that single crystals can be synthesized.

ACKNOWLEDGMENTS

Computational resources were provided by the Swiss National Supercomputing Center withing the project s970. This study was supported in part by KAKENHI (Grant No. 17H01195, 17H06137, 19H02424, and 19K14652), the

Asahi Glass Foundation, and Multidisciplinary Research Laboratory System for Future Developments. The synchrotron XRD measurement was performed with the approval of the Photon Factory Program Advisory Committee (Proposal No. 2018S2-006). We acknowledge the Center for Computational Materials Science, Institute for Materials Research, Tohoku University for the use of MASAMUNE-IMR (MAterials science Supercomputing system for Advanced MUlti-scale simulations towards NExt-generation). (Project No. 20S0023)

[1] R. J. Cava, R. B. van Dover, B. Batlogg, and E. A. Rietman, Phys. Rev. Lett. **58**, 408 (1987).

[2] J. B. Torrance, Y. Tokura, A. I. Nazzal, A. Bezinge, T. C. Huang, and S. S. P. Parkin, Phys. Rev. Lett. **61**, 1127 (1988).

[3] Y. Maeno, H. Hashimoto, K. Yoshida, S. Nishizaki, T. Fujita, J. Bednorz, and F. Lichtenberg, Nature (London) **372**, 532 (1994).

[4] A. P. Mackenzie, T. Scaffidi, C. W. Hicks, and Y. Maeno, npj Quantum Mater. **2**, 532 (2017).

[5] A. Pustogow, Y. Luo, A. Chronister, Y.-S. Su, D. A. Sokolov, F. Jerzembeck, A. P. Mackenzie, C. W. Hicks, N. Kikugawa, S. Raghu, E. D. Bauer, and S. E. Brown, Nature (London) **574**, 72 (2019).

[6] J. Matsuno, Y. Okimoto, Z. Fang, X. Z. Yu, Y. Matsui, N. Nagaosa, M. Kawasaki, and Y. Tokura, Phys. Rev. Lett. **93**, 167202 (2004).

[7] M. K. Crawford, M. A. Subramanian, R. L. Harlow, J. A. Fernandez-Baca, Z. R. Wang, and D. C. Johnston, Phys. Rev. B **49**, 9198 (1994).

[8] B. J. Kim, H. Jin, S. J. Moon, J.-Y. Kim, B.-G. Park, C. S. Leem, J. Yu, T. W. Noh, C. Kim, S.-J. Oh, J.-H. Park, V. Durairaj, G. Cao, and E. Rotenberg, Phys. Rev. Lett. **101**, 076402 (2008).

[9] C. D. Dashwood, H. Miao, J. G. Vale, D. Ishikawa, D. A. Prishchenko, V. V. Mazurenko, V. G. Mazurenko, R. S. Perry, G. Cao, A. de la Torre, F. Baumberger, A. Q. R. Baron, D. F. McMorrow, and M. P. M. Dean, Phys. Rev. B **100**, 085131 (2019).

[10] B. J. Kim, H. Ohsumi, T. Komesu, S. Sakai, T. Morita, H. Takagi, and T. Arima, Science **323**, 1329 (2009).

[11] H. Fukazawa, S. Nakatsuji, and Y. Maeno, Physica B **281-282**, 613 (2000).

[12] H. Okabe, M. Isobe, E. Takayama-Muromachi, A. Koda, S. Takeshita, M. Hiraishi, M. Miyazaki, R. Kadono, Y. Miyake, and J. Akimitsu, Phys. Rev. B **83**, 155118 (2011).

[13] M. Itoh, T. Shimura, Y. Inaguma, and Y. Morii, J. Solid State Chem. **118**, 206 (1995).

[14] R. Perry, F. Baumberger, L. Balicas, N. Kikugawa, N. Ingle, A. Rost, J. Mercure, Y. Maeno, Z. Shen, and A. Mackenzie, New J. Phys. **8**, 175 (2006).

[15] L. J. Sandilands, W. Kyung, S. Y. Kim, J. Son, J. Kwon, T. D. Kang, Y. Yoshida, S. J. Moon, C. Kim, and T. W. Noh, Phys. Rev. Lett. **119**, 267402 (2017).

[16] M. W. Haverkort, I. S. Elfimov, L. H. Tjeng, G. A. Sawatzky, and A. Damascelli, Phys. Rev. Lett. **101**, 026406 (2008).

[17] T. F. Qi, O. B. Korneta, L. Li, K. Butrouna, V. S. Cao, X. Wan, P. Schlottmann, R. K. Kaul, and G. Cao, Phys. Rev. B **86**, 125105 (2012).

[18] J. Kwon, M. Kim, D. Song, Y. Yoshida, J. Denlinger, W. Kyung, and C. Kim, Phys. Rev. Lett. **123**, 106401 (2019).

[19] F. Izumi and K. Momma, Solid State Phenom. **130**, 15 (2007).

[20] J. A. Flores-Livas, J. Phys.: Condens. Matter **32**, 294002 (2020).

[21] J. P. Perdew, K. Burke, and M. Ernzerhof, Phys. Rev. Lett. **77**, 3865 (1996).

[22] G. Kresse and J. Furthmüller, Comput. Mater. Sci. **6**, 15 (1996).

[23] K. Dewhurst *et al.*, The Elk FP-LAPW Code (2015).

[24] K. Lejaeghere, G. Bihlmayer, T. Björkman, P. Blaha, S. Blügel, V. Blum, D. Caliste, I. E. Castelli, S. J. Clark, A. Dal Corso *et al.*, Science **351**, 1415 (2016).

[25] See the supplemental material at http://link.aps.org/supplemental/10.1103/PhysRevMaterials.5.015001 for Figs. S1– S6 and Tables SI and SII.

[26] R. Shannon and C. Prewitt, J. Inorg. Nucl. Chem. **32**, 1427 (1970).

[27] K. Yamaura, Q. Huang, D. P. Young, and E. Takayama-Muromachi, Chem. Mater. **16**, 3424 (2004).

[28] S. Kittaka, S. Nakamura, T. Sakakibara, N. Kikugawa, T. Terashima, S. Uji, D. A. Sokolov, A. P. Mackenzie, K. Irie, Y. Tsutsumi, K. Suzuki, and K. Machida, J. Phys. Soc. Jpn. **87**, 093703 (2018).

[29] A. Georges, L. d. Medici, and J. Mravlje, Annu. Rev. Condens. Matter Phys. **4**, 137 (2013).

[30] T. Oguchi, Phys. Rev. B **51**, 1385 (1995).

[31] Z. Wang, D. Walkup, P. Derry, T. Scaffidi, M. Rak, S. Vig, A. Kogar, I. Zeljkovic, A. Husain, L. H. Santos, Y. Wang, A. Damascelli, Y. Maeno, P. Abbamonte, E. Fradkin, and V. Madhavan, Nat. Phys. **13**, 799 (2017).

[32] A. Tamai, M. Zingl, E. Rozbicki, E. Cappelli, S. Riccò, A. de la Torre, S. McKeown Walker, F. Y. Bruno, P. D. C. King, W. Meevasana, M. Shi, M. Radović, N. C. Plumb, A. S. Gibbs, A. P. Mackenzie, C. Berthod, H. U. R. Strand, M. Kim, A. Georges, and F. Baumberger, Phys. Rev. X **9**, 021048 (2019).

[33] N.-O. Linden, M. Zingl, C. Hubig, O. Parcollet, and U. Schollwöck, Phys. Rev. B **101**, 041101(R) (2020).

[34] Y. Hou, H. Xiang, and X. Gong, New J. Phys. **18**, 043007 (2016).

[35] C. Martins, M. Aichhorn, and S. Biermann, J. Phys.: Condens. Matter **29**, 263001 (2017).

[36] R. Arita, J. Kuneš, A. V. Kozhevnikov, A. G. Eguiluz, and M. Imada, Phys. Rev. Lett. **108**, 086403 (2012).

[37] C. Martins, M. Aichhorn, L. Vaugier, and S. Biermann, Phys. Rev. Lett. **107**, 266404 (2011).

[38] S. Moser, L. Moreschini, A. Ebrahimi, B. Dalla Piazza, M. Isobe, H. Okabe, J. Akimitsu, V. V. Mazurenko, K. S. Kim, A. Bostwick, E. Rotenberg, J. Chang, H. M. Rønnow, and M. Grioni, New J. Phys. **16**, 013008 (2014).

[39] K. Ishida, M. Manago, K. Kinjo, and Y. Maeno, J. Phys. Soc. Jpn. **89**, 034712 (2020).

[40] S. Benhabib, C. Lupien, I. Paul, L. Berges, M. Dion, M. Nardone, A. Zitouni, Z. Q. Mao, Y. Maeno, A. Georges, L. Taillefer, and C. Proust, Nat. Phys. (2020), doi: 10.1038/s41567-020-1033-3.

[41] S. Ghosh, A. Shekhter, F. Jerzembeck, N. Kikugawa, D. A. Sokolov, M. Brando, A. P. Mackenzie, C. W. Hicks, and B. J. Ramshaw, Nat. Phys. (2020), doi: 10.1038/s41567-020-1032-4.
[42] W. Witczak-Krempa, G. Chen, Y. B. Kim, and L. Balents, Annu. Rev. Condens. Matter Phys. **5**, 57 (2014).
[43] J. Wu, H. P. Nair, A. T. Bollinger, X. He, I. Robinson, N. J. Schreiber, K. M. Shen, D. G. Schlom, and I. Božović, Proc. Natl. Acad. Sci. (USA) **117**, 10654 (2020).
[44] W. Huang and H. Yao, Phys. Rev. Lett. **121**, 157002 (2018).
[45] M. Malvestuto, E. Carleschi, R. Fittipaldi, E. Gorelov, E. Pavarini, M. Cuoco, Y. Maeno, F. Parmigiani, and A. Vecchione, Phys. Rev. B **83**, 165121 (2011).
[46] G. Zhang, E. Gorelov, E. Sarvestani, and E. Pavarini, Phys. Rev. Lett. **116**, 106402 (2016).
[47] O. Gingras, R. Nourafkan, A. M. S. Tremblay, and M. Côté, Phys. Rev. Lett. **123**, 217005 (2019).
[48] J. J. Deisz and T. E. Kidd, Phys. Rev. B **95**, 045122 (2017).
[49] C. K. Poole, H. A. Farach, and R. J. Creswick, *Handbook of Superconductivity* (Elsevier, Amsterdam, 1999).
[50] D. Pesin and L. Balents, Nat. Phys. **6**, 376 (2010).